

# Graphene-based reconfigurable FSS for dynamic millimeter-wave OAM beam generation

Nidal Qasem

Department of Communications and Computer Engineering, Faculty of Engineering, Al-Ahliyya Amman University, Amman, Jordan

## Article Info

### Article history:

Received Jan 5, 2025

Revised Apr 15, 2025

Accepted Jul 3, 2025

### Keywords:

Frequency selective surface

Graphene

IRM

Millimeter wave

OAM

Wireless communications

## ABSTRACT

This research paper explores the dynamic generation of orbital angular momentum (OAM) beams at millimeter-wave (mm-wave) frequencies using intelligent reconfigurable metasurfaces (IRM). The ability to dynamically control OAM properties is crucial for unlocking these beams' full potential. This paper proposes a novel method utilizing a frequency-selective surface (FSS) integrated with reconfigurable graphene to generate an IRM. By carefully designing the FSS elements and controlling the graphene's electrical conductivity, the system can generate and manipulate mm-wave OAM beams with different topological charges. With the suggested IRM structure, a conversion efficiency of nearly 80% can be achieved in converting the circularly polarized incident wave into its cross-polarized component at 30.7 GHz, with an overall thickness of  $0.067 \lambda$ . This research has significant implications for advancing mm-wave communications by providing additional spatial dimensions for multiplexing and enhancing system capacity.

This is an open access article under the [CC BY-SA](https://creativecommons.org/licenses/by-sa/4.0/) license.



## Corresponding Author:

Nidal Qasem

Department of Communications and Computer Engineering, Faculty of Engineering

Al-Ahliyya Amman University

Amman, Jordan

Email: ne.qasem@ammanu.edu.jo

## 1. INTRODUCTION

The generation and manipulation of orbital angular momentum (OAM) beams at millimeter-wave (mm-wave) frequencies have attracted growing interest and research in recent years. OAM waves are a type of electromagnetic wave characterized by a rotating wavefront. They possess a twisted or helical shape, unlike traditional plane waves. OAM is associated with the spatial phase distribution of the wave and is quantified by an integer value called the topological charge. Different OAM modes with distinct topological charges can carry independent information, offering significant advantages for a range of technological applications, including high-speed wireless communications, advanced radar systems, and cutting-edge imaging techniques [1], [2].

The capacity to dynamically control the OAM properties of mm-wave beams is a key enabler for unlocking the full potential of these specialized electromagnetic waves [3]. There are several promising ways to achieve this dynamic control, such as using a spiral phase plate [4], a uniform circular array [5], transmit arrays [6], and a metasurface (MS) or frequency selective surface (FSS) [7], [8].

An FSS, consisting of subwavelength engineered structures, offers a promising approach for generating mm-wave OAM waves. By carefully designing the FSS elements, the phase and amplitude of incident waves can be controlled, enabling the generation of OAM beams.

Several studies have presented advancements in the MS field, including the introduction of a new method based on a microwave FSS to develop a low-level vortex beam generator that can produce an OAM mode under circular polarization [9]. Additionally, ultra-thin MSs have been created, produced, and characterized to efficiently generate electromagnetic waves that convey OAM waves at microwave frequencies. Based on the photonic spin Hall effect, a subwavelength scatterer with a transmission efficiency of up to 85% was developed. The scatterer's spatial rotation was utilized to provide phase control between 0 and  $2\pi f$  [10]. Another study focused on an azimuthally symmetric electromagnetic MS with wide bandwidth designed, fabricated, and experimentally demonstrated to efficiently convert a left-handed (right-handed) circularly polarized incident plane wave (with a spin angular momentum of  $\hbar$ , where  $\hbar$  is the reduced Planck's constant) to a right-handed (left-handed) circularly polarized vortex wave with OAM. The simulation and measurement results confirmed that the proposed method provides an effective way of generating an OAM-carrying vortex wave with comparative performance across a broad bandwidth [11]. In addition, a transmitting MS with ultra-high polarization conversion capabilities and conveying OAM vortex waves was proposed based on the distinct periodic unit cell structure of the mm-wave. The findings demonstrate the benefits of vortex waves, which include high mode purity, bandwidth, and efficiency. Fast beam alignment is possible with the generated vortex waves, which is important for mm-wave satellite communications and unmanned aerial vehicles [12]-[14]. By incorporating reconfigurable components, such as graphene [15], [16], into the FSS design, dynamic adjustment of the beam's OAM properties in real-time is possible, enabling advanced beam-shaping capabilities [17].

Graphene, a remarkable two-dimensional material with exceptional electrical and optical characteristics, has emerged as a valuable material for integration into reconfigurable FSSs. Its tunable electrical conductivity, which is controlled by applying a bias voltage, allows for the dynamic manipulation of the FSS's electromagnetic response, leading to the generation of reconfigurable mm-wave OAM beams [18]. The unique properties of graphene, including its high carrier mobility, tunability, and broadband response, make it an attractive choice for integration with FSSs to achieve dynamic control over mm-wave OAM beams [19].

This paper investigates the development of an OAM generator, which involves designing an FSS and integrating reconfigurable graphene to form intelligent reconfigurable metasurfaces (IRM). A third-order bandpass FSS that operates under circularly polarized light and is primarily dependent on the coupling between the metallic layers was constructed. It comprised stacked patches and grids divided by thin dielectric substrates. The suggested unit cell had a high transmission efficiency operating bandwidth and approximately 100% conversion efficiency at the center frequency when compared to resonant elements. Additionally, reconfigurable graphene was also exploited to include all phases in a single cell and the ability to operate only one phase each time, forming an IRM. The working concept of this IRM design was examined by utilizing an analogous circuit model. To adjust the transmitted cross-polarized component's wavefront, the Pancharatnam-Berry (PB) phase was incorporated. With a thickness of only  $0.067 \lambda$ , the ultra-thin OAM-producing device is intended for mm-wave operation. The creation of an extremely effective vortex beam carrying the OAM mode in the passband was confirmed by both simulation and experimental data. Additionally, by determining the purity of several high OAM modes, I explored the bound of the OAM topological charge number attained with the suggested finite-size OAM generator.

The paper is organized as follows: section 2 provides an overview of the proposed system and the design details of the reconfigurable surface, while section 3 discusses the simulation results using tools such as MATLAB and CST Studio Suite. Finally, the conclusions are summarized in section 4.

## 2. SYSTEM MODEL

The key objective was to design an IRM through which OAM waves are transmitted in different modes orthogonal to each other. The desired results have been obtained using MATLAB and CST Studio Suite. In this section, the following elements have been described as: the overall working principle, the design of the FSS unit cell and implementation of IRM, the working principle of graphene, the generation of OAM waves, and the degree of purity.

### 2.1. Principle of operation

The idea behind the proposed IRM that produces cross-polarization under circularly polarized incident wave illumination is shown in Figure 1. As an anisotropic structure, the unit cell can react differently to incident waves that are polarized in both the  $x$ - and  $y$ -axis directions. At a particular transmission phase difference, the two transmission bands overlap at frequency  $f_0$ , where the ideal transmission coefficients equal 1. The transmission matrix for an incident wave that is circularly polarized is written as [9], [20]:

$$T_{CP} = \begin{pmatrix} T_{LL} & T_{LR} \\ T_{RL} & T_{RR} \end{pmatrix} = \begin{pmatrix} \frac{T_{xx}+T_{yy}+i(T_{xy}-T_{yx})}{2} & \frac{T_{xx}-T_{yy}-i(T_{xy}+T_{yx})}{2} \\ \frac{T_{xx}-T_{yy}+i(T_{xy}+T_{yx})}{2} & \frac{T_{xx}+T_{yy}-i(T_{xy}-T_{yx})}{2} \end{pmatrix} \quad (1)$$

Thus, for an incident right-hand (left-hand) circularly polarized wave,  $T_{RL}$  ( $T_{LR}$ ) is the complex cross-polarized transmission coefficient of the left-hand (right-hand) circularly polarized component. For left- and right-handed circularly polarized incident waves, respectively,  $T_{LL}$  and  $T_{RR}$  correspond to the complex co-polarized transmission coefficients. Likewise, the complex transmission coefficients for an incident linearly polarized wave are denoted by  $T_{xx}$ ,  $T_{xy}$ ,  $T_{yx}$ , and  $T_{yy}$ . For the unit's linearly polarized incident wave, the cross-polarized transmission coefficients are typically regarded as insignificant, with  $T_{xy} = T_{yx} = 0$ . Consequently,  $T_{xx}$  and  $T_{yy}$  have a major influence on the capacity to convert polarization in a circular manner [9]. For an incident wave with a left-handed circular polarization (LHCP) is:

$$T_{RL} = T_{xx} - T_{yy} = |T_{xx}| e^{-j\phi_{xx}} \frac{1 + \frac{|T_{yy}|}{|T_{xx}|} e^{j(\phi_{xx} - \phi_{yy} - \pi)}}{2} \quad (2)$$

where  $\phi_{xx}$  and  $\phi_{yy}$  denote the transmission phase of the incident linearly polarized wave. Consequently, for the circularly polarized wave, the optimal cross-polarized conversion condition is:

$$|T_{xx}| = |T_{yy}| = 1 \quad (3a)$$

$$\phi_{xx} - \phi_{yy} = \pi \quad (3b)$$

This results in a 100% conversion efficiency since the unit cell has the same transmission efficiency in both directions without experiencing any loss. Additionally, if the aforementioned conversion requirements are not strictly met, the transmitted wave still contains a cross-polarized component, but it does so with less efficiency.

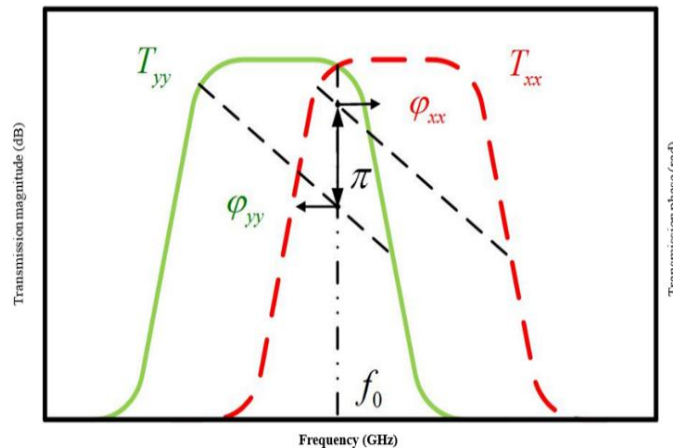


Figure 1. The cross-conversion of circularly polarized waves in the proposed IRM unit cell

## 2.2. Design of the FSS unit cell and implementation of IRM

The three-dimensional (3D) view of a primary cell in the FSS architecture is presented in Figure 2. Using a circular grid with a rectangular patch loaded in the circular gaps, a capacitively coupled miniaturized-element FSS (MEFSS) is first used to build the structure. A class of non-resonant periodic multi-layered structures known as general MEFSS is composed of several metallic layers divided by thin dielectric substrates. Every metallic layer is either a two-dimensional (2D) wire grid with sub-wavelength periodicity or a 2D periodic arrangement of sub-wavelength patches [21]-[23]. A thorough synthesis and analytical design process for the MEFSS is documented in [24].

This technique was originally used to develop a second-order bandpass response MEFSS. Next, a circular grid replaces the wire grid to introduce the PB phase by rotating the unit cell. Rectangular patches produce two separate frequency responses for the incident circularly polarized wave's vertical ( $y$ -axis) and horizontal ( $x$ -axis) components. The maximum coverage of the transmission phase was less than  $\pi$  within a second-order bandpass MEFSS. According to (3), the phase condition of the circularly polarized conversion was not satisfied in this case.

The MEFSS unit usually acts as a spatial phase shifter, increasing the phase shift variation as the increase in response order. Therefore, a rectangular patch is embedded in the center of the circular gaps to add another order for the equivalent filter circuit. Because of the strong coupling of the gap between the rectangular patch and the arc grid in the vertical direction, the unit cell presents an extra resonance compared to the other direction. All patches are symmetric to provide different capacitive values in the two orthogonal directions, and the arc grid is symmetric to provide the same inductance value. The dimensions of the unit cell along the  $x$ - and  $y$ -axis directions are  $D_x = D_y = D$ , while the thicknesses of both substrates are the same ( $h_1 = h_2$ ), as shown in Figures 2(a) and 2(b). Owing to the vertically symmetrical structure, the top and bottom metallic layers of the unit cell comprise the same sub-wavelength capacitive rectangular patches with dimensions  $P_{x1} \times P_{y1}$  and  $P_{x2} \times P_{y2}$ . The radius of the circular gaps in the middle metal layer is  $R$ , while the length along the  $x$ - and  $y$ -axis directions of the middle rectangular patch are  $P_{x3}$  and  $P_{y1}$ , respectively, as shown in Figure 2(c).

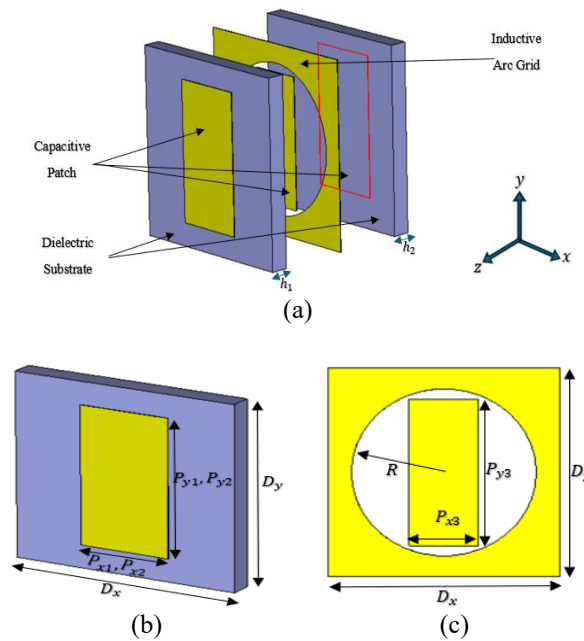


Figure 2. FSS primary cell; (a) content of the cell, (b) capacitive layer top view, and (c) middle layer top view

To enhance comprehension of the structure's working principle, a generalized equivalent circuit model (ECM) is suggested, as shown in Figure 3. As seen in Figure 3(a), the components of the analogous circuit model are the same for both orthogonal polarizations. The circular grid is viewed as an inductor  $L_x$ , and the rectangular patches are regarded as capacitors  $C_{x1}$ ,  $C_{x2}$ , and  $C_{x3}$  for the  $x$ -axis direction and  $C_{y1}$ ,  $C_{y2}$ , and  $C_{y3}$  for the  $y$ -axis direction. The corresponding capacitor is parallel to the grid's inductor because the rectangular patch is embedded in the circular gap. A series inductor ( $L_{T1}$ ,  $L_{T2}$ ) and a shunt capacitor ( $C_{T1}$ ,  $C_{T2}$ ) can be used in the model to represent the short transmission lines that are equivalent to the thin dielectric substrates separating each metallic layer. Free space characteristic impedances  $Z_0 = 377 \Omega$  can be used to represent the half spaces on either side of the unit cell structure. As Figure 3(b) illustrates, the circuit model is a third-order bandpass filter. Capacitors  $C_{x1}$ ,  $C_{x2}$ , and inductors  $L_{T1}$ ,  $L_{T2}$ , respectively, make up two of the resonators. The intermediate layer resonator is made up of a parallel capacitor  $C_{x3}$  and the inductor  $L_x$ .

The specific values of the capacitors in the metallic patches can be explained as follows based on the ECM of this structure [24]:

$$C_i = \varepsilon_0 \varepsilon_{eff} \frac{2D}{\pi} \ln \left( \frac{1}{\sin \frac{\pi S_i}{2D}} \right) \quad (4)$$

where  $\varepsilon_0$  is the vacuum permittivity ( $F/m$ ),  $\varepsilon_{eff}$  is the dielectric substrate's effective permittivity,  $D$  is the unit cell's periodicity, and  $S_i$  is the space between two consecutive patches. Similarly, the following can be used to characterize the particular inductive value of metallic grid wires [24]:

$$L_i = \mu_0 \mu_{eff} \frac{D}{2\pi} \ln \left( \frac{1}{\sin \frac{\pi W_i}{2D}} \right) \quad (5)$$

where  $\mu_0$  is the vacuum permeability,  $\mu_{eff}$  is the effective permeability of the dielectric substrate, and  $W_i$  is the effective width of the arc grid that is impacted by the patch embedded in the circular gap. One may compute the dielectric substrate's equivalent inductor and capacitor from:

$$L_{Ti} = \mu_0 \mu_{eff} h_i \quad (6a)$$

$$C_{Ti} = \varepsilon_0 \varepsilon_{eff} h_i \quad (6b)$$

where the equivalent inductance and capacitance of the dielectric substrates are denoted by  $L_{Ti}$  and  $C_{Ti}$ , respectively. Subsequently, a cell design has been proposed to cover all phases. The three rectangular patches have been rotated around the  $z$ -axis with a step of  $\pi/12$ , to obtain the seven phases within the unit cell, and each time, three patches are chosen for one phase. The cross-polarization transmission coefficient is as large as possible at 30.7 GHz. The transport phase is obtained with the same phase gradient of  $\pi/6$ , approximately twice the rotation angle, which corresponds to the PB phase.

Figure 4 displays the 3D view of the primary unit cell in the proposed IRM design. The FSS design described previously was built, but it has been changed by replacing the three rectangular copper patches with rectangular graphene patches and combining all their phases into one cell, as shown in Figure 4(a). Where Figures 4(b) and 4(c) show the top view for the capacitive and middle layers, respectively. After that, one phase has been activated at a time depending on the desired shape of the metasurface. This material can be controlled by introducing a constant current to change the surface impedance of the graphene layers ( $Z_s$ ), thus turning them ON and OFF (i.e.  $Z_{ON}/Z_{OFF}$ ) using this current. This technique will be clarified in the next section.

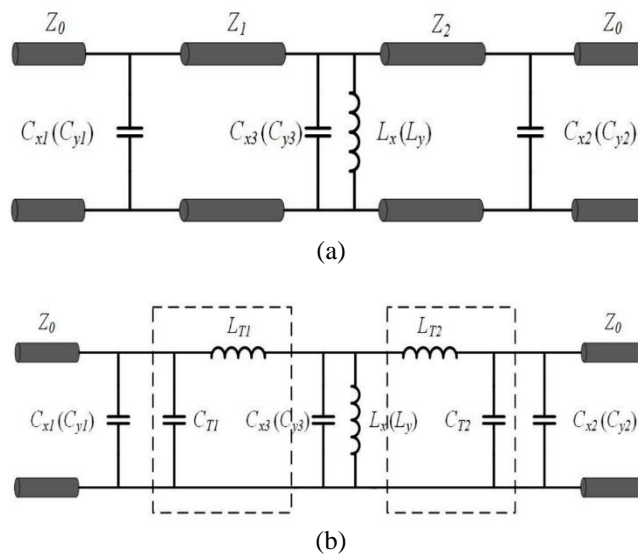


Figure 3. The FSS unit cell's ECM structure (a) it should be noticed that the ECM is the same for  $x$ - and  $y$ -polarizations expect for the values of the capacitor and inductor and (b) the simplified ECM by considering the transmission line as a shunt capacitor and inductor

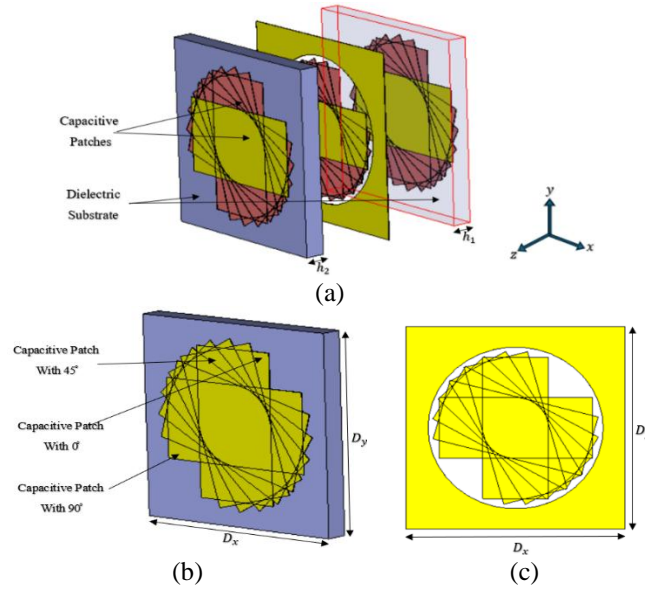


Figure 4. Proposed IRM primary cell; (a) content of the cell, (b) capacitive layer top view, and (c) middle layer top view

### 2.3. Graphene

The conductivity of graphene varies between the microwave and THz frequency ranges. In the microwave frequency range, graphene has a middling conductivity with a short tunability range, while in the THz frequency range, it has better conductivity with a large tunability range. Frequency-tunable metallic antennas can be facilitated by the special tunable feature conductivity of graphene [25]. In our work, the graphene's alternating current conductivity can be expressed as follows [26], [27]:

$$\sigma_{AC} = \frac{-jq^2k_BT}{\pi\hbar^2(\omega - j\tau_t^{-1})} \left( \frac{\mu_c}{k_BT} + 2 \ln \left( e^{-\frac{\mu_c}{k_BT}} + 1 \right) \right) \quad (7)$$

where  $\omega$  is the radian frequency ( $rad/sec$ ),  $\mu_c$  is the chemical potential ( $eV$ ),  $\tau_t$  is the relaxation time ( $s$ ),  $T$  is the temperature in Kelvin ( $K$ ),  $q$  is the elementary charge ( $C$ ),  $\hbar$  is the reduced Planck's constant ( $J/s$ ), and  $k_B$  is the Boltzmann constant ( $J/K$ ). The chemical potential of graphene is linked to the carrier density  $n$  ( $m$ ) and can be obtained from the following:

$$\mu_c = \hbar v_f \sqrt{n\pi} \quad (8)$$

where  $v_f$  is the Fermi velocity of graphene and equal  $1 \times 10^6$  ( $m/s$ ). The value of  $n$  can be sequentially adjusted by applying an external DC voltage on the graphene layer and the value of  $n$  can be obtained from the following:

$$n = \frac{\epsilon_0 \epsilon_r V_b}{dq} \quad (9)$$

where  $\epsilon_r$  is the relative dielectric constant,  $V_b$  is the external DC bias voltage ( $V$ ),  $d$  is the graphene layer thickness ( $m$ ). The graphene surface impedance ( $Z$ ) can be calculated from the graphene conductivity as follows [26], [27]:

$$Z_s = \frac{1}{\sigma_{AC}} \quad (10)$$

$$Z_s = \frac{j\pi\hbar^2(2\pi f(\tau_l\tau_s) - j(\tau_l + \tau_s))}{q^2(\tau_l\tau_s)[\mu_c + 2k_BT \ln(e^{-\frac{\mu_c}{k_BT}} + 1)]} \quad (11)$$

The scattering effects  $\tau_l$  can be calculated as follows:

$$\tau_l = \frac{\mu_l \hbar \sqrt{n\pi}}{qv_f} \quad (12)$$

where  $\mu_l$  is the mobility electron ( $m^2/V_s$ ). The value of  $\tau_s$  can be calculated as follows:

$$\tau_s = \frac{4\hbar^2 \rho_m v_{ph}^2 v_f}{\sqrt{n\pi} k_B T D_p^2} \quad (13)$$

where  $\rho_m$  is the 2D mass density of graphene and equal  $7.6 \times 10^{-6}$  ( $Kg/m^2$ ),  $v_{ph}$  is the sound velocity of the longitudinal acoustic phonons in graphene and equal  $2.1 \times 10^4$  (m/s), and  $D_p$  is the deformation potential (eV). However, in some experimental values from previous studies, the  $R$  value around  $\sim 18$  eV is a prevalent and recognized value for graphene over a substrate [27].

#### 2.4. Generation of OAM and the purity of modes

The FSS is a metasurface with a square aperture consisting of  $20 \times 20$  elements and a horn antenna placed on the central axis of the left side, as seen in Figure 5. The horn antenna is a circularly polarized feed antenna so that the spherical wave from this antenna is fed to the FSS surface on the  $z$ -axis to obtain a vortex wave. Considering that the position of the antenna is  $(x_f, y_f, z_f)$  and the position of each element is  $(x_i, y_j)$ , the following equation can be applied to obtain the value of  $\theta$  [9], [12]:

$$\theta = l \tan^{-1} \frac{y_i}{x_i} - k_o \left[ \sqrt{(x_i - x_f)^2 + (y_i - y_f)^2 + z_f^2} - z_f \right] \quad (14)$$

where  $l$  is the predicted OAM mode and  $k_o$  is the free space propagation constant. For each metallic layer, the rectangular patches must be rotated by  $\theta$  in accordance with their corresponding azimuth to meet the requirements of the PB phase [9]. The first section is the OAM wave, so the required mode is carried by the transmitted wave. The second section is the phase compensation, which compensates for the phase variation caused by the variation in wave range. The desired phase for the periodic cell is found by deducting the phase compensation part from the OAM vortex part [12].

Figure 5 shows the configuration employed for the simulation. Two monitors were utilized in the simulations; one is placed in the  $xoy$  plane at  $z = 10$  mm, and the other is placed along the propagation direction at  $y = 0$  mm in the  $xoz$  plane. The boundary condition is set to the perfectly matched layer.

The proposed system for generating the OAM model was examined in terms of its purity. To conduct a Fourier transform analysis, the transmission magnitude field toroidal E-field surrounding the null-magnitude point is taken individually [28]:

$$A_l = \frac{1}{2\pi} \int_0^{2\pi} \omega(\varphi) e^{-jl\varphi} d\varphi \quad (15)$$

$$\omega(\varphi) = \sum_l A_l e^{jl\varphi} \quad (16)$$

where  $\omega(\varphi)$  denotes a function of the sampling field and  $A_l$  is the intended mode's magnitude. The purity of OAM can be expressed as the ratio of each model component to the overall energy.

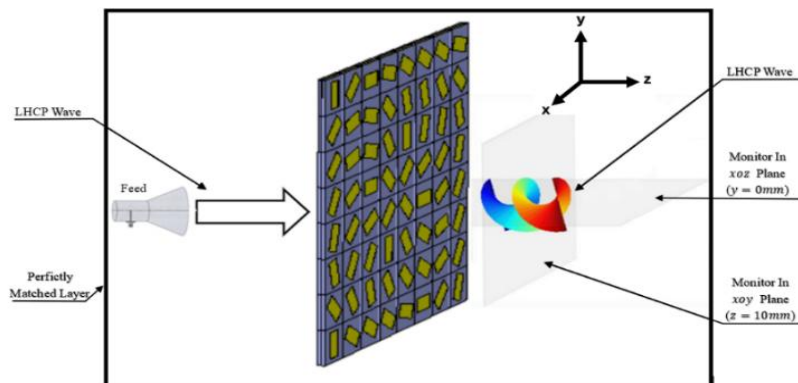


Figure 5. The simulation condition. The wave incident is an LHCP wave. By utilizing the  $xoy$  and  $xoz$  planes, the transmitted field is investigated



### 3. RESULT AND DISCUSSION

#### 3.1. FSS unit cell

Table 1 summarizes the FSS unit cell's physical dimensions and ECM component values. Using (4) to (6), the values of the capacitors and inductors are first determined. The real capacitance and inductance values rise as a result of the interaction between the three closely spaced metal layers. Additionally, there is a high electromagnetic coupling between the circular grid and the intermediate layer's rectangular patch owing to their near proximity in the vertical direction, which raises the values of capacitance and inductance. Achieving unity transmission of cross-polarization under circularly polarized incidence is the primary objective of the optimization method.

Table 1. ECM Parameters of the FSS with  $\epsilon_r = 3$

Parameter	$P_{x1}, P_{x2}$	$P_{x3}$	$P_{y1}, P_{y2}$	$P_{y3}$
Value	4 mm	3 mm	7.5 mm	7 mm
Parameter	$C_{x1}, C_{x2}$	$C_{x3}$	$C_{y1}, C_{y2}$	$C_{y3}$
Value	0.053 pF	0.0817 pF	0.192 pF	7.11 pF
Parameter	$L_x$	$L_y$	$C_{T2}$	$C_{T1}$
Value	1.929 nH	0.3401 nH	0.0825 pF	0.09 pF
Parameter	$R$	$h_1, h_2$	$L_{T1}$	$L_{T2}$
Value	4 mm	1 mm	0.140 nH	0.168 nH

The unit cell's period,  $D = 3 \text{ mm}$ , is roughly equal to  $\lambda_0/3$ , where  $\lambda_0$  is the free space wavelength at the 30.7 GHz center operation frequency. It is important to note that even while the OAM generator's design was influenced by the use of the MEFSS, the  $2\pi$  phase shift needed for OAM creation causes the cells to grow in comparison to the regular MEFSS.

The impedance values ( $Z_s$ ) of graphene have been calculated in the ON and OFF states by increasing or decreasing the charge carrier density of graphene using (12). Table 2 shows the parameter values used to obtain  $Z_{ON}$  and  $Z_{OFF}$ . The graphene layers in the unit cell were then placed at a suitable accumulated surface current position to avoid mismatch of the graphene layers in the OFF state. The IRM has been simulated via the CST Studio Suite. Figure 4 displays the dimensions of the proposed IRM.

Figure 6 shows the simulated and calculated transmission characteristics of an elementary cell. The transmission and reflection coefficients for both the horizontal and vertical linear polarizations are presented in Figure 6(a), which is based on the ECM displayed in Figure 3(b) and those generated in full-wave electromagnetic simulations using the commercial solver CST Studio Suite. Figure 6(b) displays the phase difference between the transmission phases of the two polarizations. A good agreement between the simulation results and corresponding ECM calculations is evident. Within the passband, the transmission efficiency for both the  $x$ - and  $y$ -polarized occurrences is close to 100%. On the other hand, the  $x$ - and  $y$ -axis direction response order is not matched. This is mostly caused by the short width of the middle layer's rectangular patch in the  $x$ -direction ( $P_{x3}$ ), which results in a very small capacitance value with a noticeable impact on the circuit resonance. There is a partial overlap in the transmission window for both polarizations. Owing to the different orders of response of the two perpendicular directions, the phase difference between the two directions increases stepwise. In the meantime, there is a phase shift of about  $\pi$  in the overlapped frequency band's center. As shown, there are still cross-polarization components in the transmission when  $T_x$  and  $T_y$  decrease and the phase difference deviates from  $\pi$ , but with a slightly reduced efficiency.

Then, the unit cell's behavior under circular polarization is examined, as shown in Figure 7. There is an LHCP wave tuned to the incident wave. The unit cell is rotated by a step of  $\pi/12$  around the  $z$ -axis, and the transmission coefficient of the cross-polarized wave is displayed in Figure 7(a). It is evident that when the unit cell rotates, the cross-polarization transmission efficiency of the seven units in the passband essentially stays constant. An LHCP wave can be converted by the unit to a cross-polarized wave where the cross-polarized transmission coefficient's amplitude is near 0 dB at 30.7 GHz and less than -1 dB between 30.3 and 31.2 GHz. Furthermore, the transmission phase has the same phase gradient of  $\pi/6$ , which is compatible with the PB phase and roughly double the rotation angle [9], as seen in Figure 7(b).



Table 2. ON and OFF case of impedance

Parameter	ON			OFF
$n(m^{-2})$	$8.3 \times 10^{16}$	$1.66 \times 10^{17}$	$3.3 \times 10^{17}$	$8.3 \times 10^{14}$
$V_b(V)$	5	10	20	0.05
$\mu_l(m^2/V_s)$	2.7	2.7	2.7	2.7
$D_p(eV)$	6.4	6.4	6.4	6.4
$T(K)$	295	295	295	295
$Z_s$	$29.3472 + 4.8804i$	$15.3973 + 3.4510i$	$8.4224 + 2.4402i$	$2056 + 35.126i$

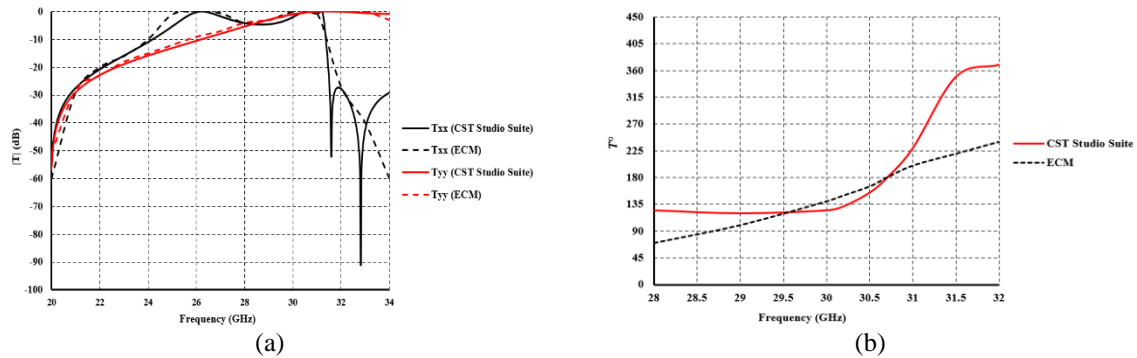


Figure 6. Calculated and simulated transmission properties of an elementary cell; (a) transmission coefficients for  $x$ - and  $y$ -axis polarization and (b) the difference in transmission phases between the two orthogonal directions

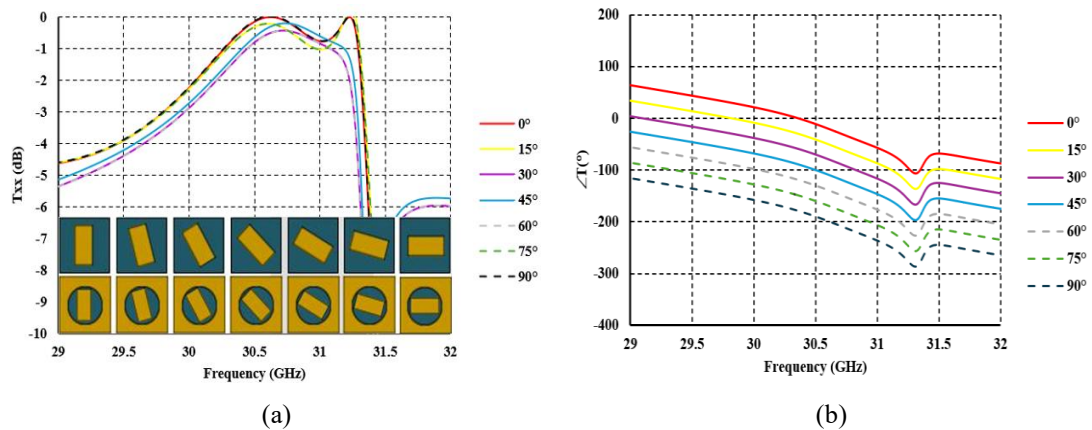


Figure 7. The cross-polarized components in normal circularly polarized incidence where the rectangular patches are rotated within a unit cell; (a) transmission coefficients and (b) the phase shift

### 3.2. Generation of OAM beam

The numerical solution simulation has been analyzed for (14) in MATLAB at 30.7 GHz, as shown in Figure 8. The equation was divided into two parts: the first section shows the OAM waves as seen in Figure 8(a), and the other shows the phase compensation in Figure 8(b). The subtraction process was performed between them, and the results are shown in Figure 8(c). The numerical solution obtained excellent OAM characteristics and high directivity of the phase distribution of the transmitted wave when the order was taken as  $l = +2$ .

Figure 9 shows the simulated results for the magnitude and phase distributions of the cross-polarized component for the FSS at  $z = 10 \text{ mm}$  under a normal LHCP incident plane wave at frequency 30.7 GHz, where Figures 9(a) and 9(b) show the results of the magnitude and phase distributions at the same frequency, respectively. It is evident that the cross-polarized component's center of energy is null, and the distribution of energy resembles a doughnut, which is one of the main characteristics of the vortex beam. The spiral gradient phase of the vortex beam in the propagation direction cross-section shows two spirals moving inside  $2\pi$  in a clockwise orientation, suggesting that the vortex beam has a topological charge of 2 [9].

The OAM purity spectrum seen in Figure 10 represents the power distribution of the transmitted wave in various OAM modes. In the simulation, the purities of the +2 OAM order mode are almost 92%. A higher order OAM mode can likewise be produced with the FSS unit cell. If the FSS array structure is big enough, this can be accomplished. On the other hand, a finite-sized OAM generator consists of a set quantity of unit cells. The structure must be split equally into  $l$  pieces, with the phase coverage of  $2\pi$  required in each part to produce an OAM mode with the topological charge  $l$ .

Here, the proposed IRM has also been analyzed, as shown in Figure 4. Figure 11 shows the simulated results for the magnitude and phase distributions of the proposed IRM. However, in Figure 11(a) the center of energy of the cross-polarized component is null, and the energy distribution is somewhat similar to the FSS with minor changes, where Figure 11(b) shows the phase distribution at the same frequency. Furthermore, the power distribution of the transmitted wave in different OAM modes in the OAM purity spectrum with the proposed unit cell was performed with the regular cell, as shown in Figure 12. The mode purity for  $l = +2$  OAM order is nearly 83% in the simulation.

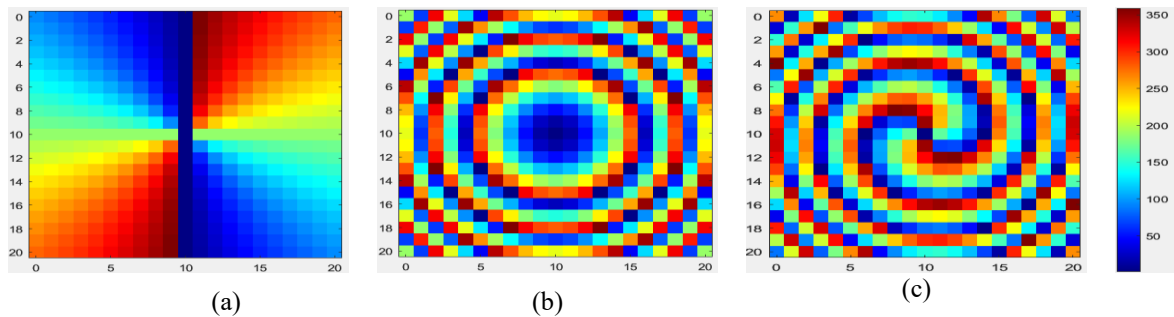


Figure 8. MATLAB representation of the phase distribution with  $l = 2$  at 30.7 GHz; (a) OAM wave, (b) phase compensation, and (c) subtraction

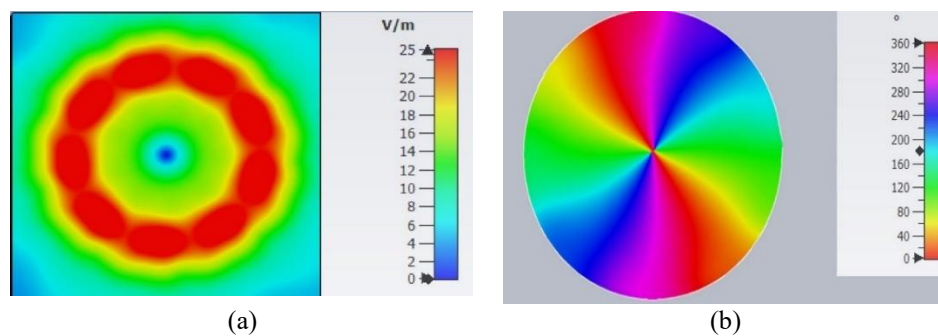


Figure 9. Simulated results for the magnitude and phase distributions of the cross-polarized component for the FSS with incidence plane wave LHCP at 30.7 GHz. (a) magnitude and (b) phase distributions in the  $xoy$  plane for  $z = 10$  mm

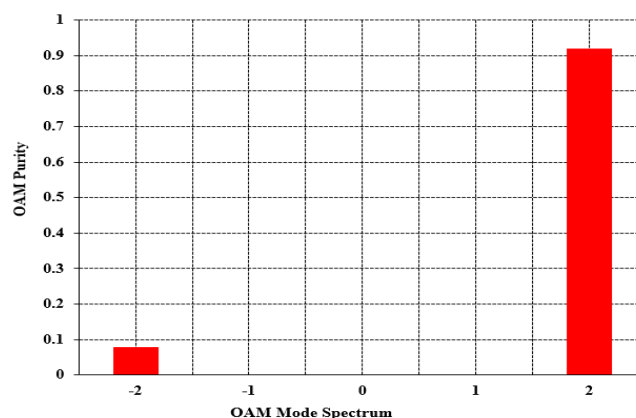


Figure 10. FSS power distribution for the +2 mode OAM generator at 30.7 GHz

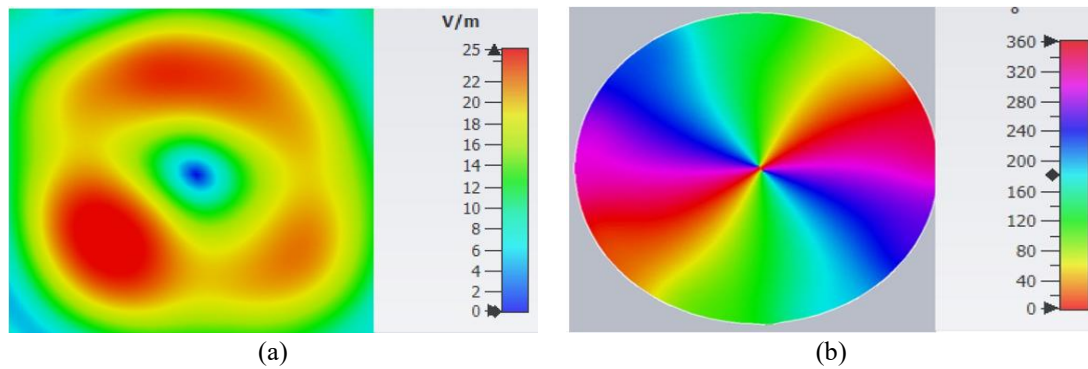


Figure 11. Simulated results for the magnitude and phase distributions of the proposed IRM; (a) magnitude distribution and (b) phase distribution

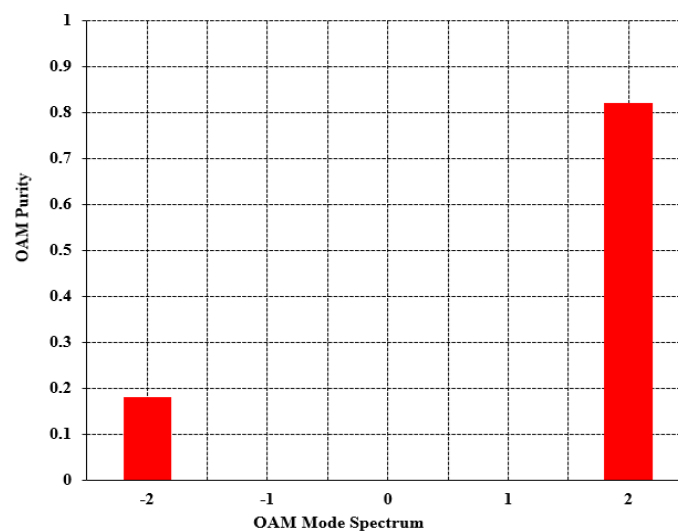


Figure 12. Proposed IRM power distribution for the +2 mode OAM generator at 30.7 GHz

In Figure 13, the simulated transmission efficiencies for the FSS and the proposed IRM, shown in Figures 2 and 4, respectively, are evaluated and illustrated. These efficiencies are defined as the ratio of the power of the cross-polarized component that introduces the OAM mode to the total incident wave power. For the FSS, during the range of 30-31.5 GHz, the transmission efficiency of the cross-polarized component exceeds 60% and reaches 87% at 30.7 GHz. While with IRM, the simulated transmission efficiency exceeds 60% at 30-31.3 GHz, and reaches 82% during 30.7 GHz. These are attributed to the excellent transmission efficiency and the precise phase difference  $\pi$  of the periodic unit cell of the IRM.

To illustrate the advantages of this scheme, the proposed IRM is compared with the designed OAM planner antenna in Table 3. The proposed IRM's advantage combines high transmission efficiency reaches 82%, high purity is nearly 83% and small aperture size. Although, Lin *et al.* [29] has high transmission efficiency, the aperture size is large, and the purity is very low. Wang *et al.* [30], the transmission efficiency is low, and the purity is unknown. Qin *et al.* [31], a transmission phase design based on transmit arrays (TAs) with a strong chromatic response leads to a narrow operating band and the transmission efficiency is very low. Where both obtain a low transmission efficiency, and low purity [9], [10]. Wang *et al.* [32], controlled PIN ON/OFF is employed to generate multiple transmissive OAM waves in the  $\pm 1$ ,  $\pm 2$ ,  $\pm 3$  and  $\pm 4$  modes, though the resulting purity is low and the transmission efficiency is unknown. Moreover, the periodic unit cell has a phase-modulated, 13-layer PIN reconfigurable architecture with a  $2.6\lambda$  profile height. Jiang *et al.* [11] shows a fairly high transmission efficiency in the X-band but suffers from the problem of a very large aperture area. Yu *et al.* [12] suggested a transmitting metasurface (TMS) that features slightly high transmission efficiency and purity, and middle aperture size. In the proposed system, the numerical simulation results are very consistent showing that the demonstrated IRM, with its reconfigurability and easy phase control, can

generate high-purity vortex waves stably and efficiently considering the high efficiency, broadband, and low aperture area size. This vortex wave can prevent beam shift and misalignment and utilize the advantages of OAM waves well, which are applied to achieve OAM multiplexing and fast alignment in the Ka-band.

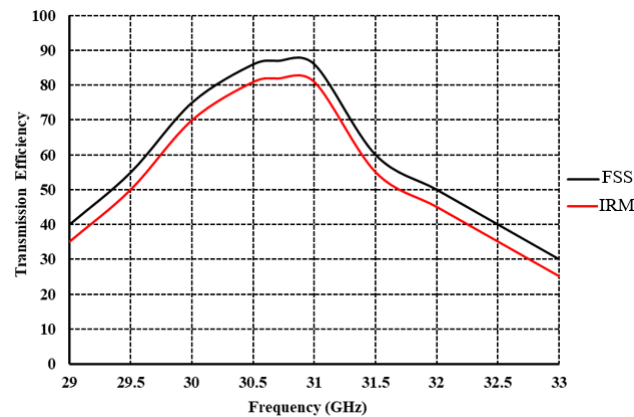


Figure 13. Transmission efficiency

Table 3. Performance comparison of the proposed designed IRM with that of the current OAM planar antenna

Ref	Antenna type (Polarization)	Frequency Bands (GHz)	Aperture size ( $\lambda$ )	OAM modes	Reconfigurability	Efficiency (%)	OAM Purity (%)
[29]	Meta-lens (LP)	26.5-40.0	12.2×12.2×2.2	1	No	59.5-86.2	>50.0
[30]	ME-FSS (LP)	10.6	8.5×8.5×0.2	1	No	> 60.0	
[31]	TAs (LP)	10.0	8.0×8.0×0.2	1	No	11.9	>81.5
[32]	PIN Reconfigurable (-)	10.0	6.9×7.3×2.6	$\pm 1$ & $\pm 2$ & $\pm 3$ & $\pm 4$	Yes	—	>60 & >60 & 50 & 40
[9]	FSS (CP)	10.0-11.1	12.5×12.5×0.1	2	No	>50.0	93.4
[10]	TMS (CP)	10.0	6.0×6.0×0.1	1	No	54.0	—
				2		39.0	
[11]	TMS (CP)	7.5-10.5	Circle with diameter $12\lambda$	2	No	60.0	—
[12]	TMS (CP)	17-19	9.6×9.6×0.1	$\pm 1$ & $\pm 2$ & $\pm 3$	No	64.4	>70.8
Prop.	IRM (CP)	30-31.3	6.67×6.67×0.067	Depends on the number of unit cells	Yes	>82	>83

#### 4. CONCLUSION

The feasibility of dynamically generating and controlling OAM beams at mm-wave frequencies has been successfully demonstrated. By integrating reconfigurable graphene with a FSS, an IRM was designed and analyzed. The IRM enabled precise control over the phase and amplitude of the incident electromagnetic wave, leading to the generation of OAM beams with different topological charges. In the regular FSS, when  $l = +2$ , the OAM order's mode purity was almost 92%, while the OAM purity spectrum with the proposed IRM was nearly 83% in the simulation at the same order, while the transmission efficiency of 87% and 82% have been achieved, respectively.

In addition, the bound of the order of OAM mode that can be generated by a fixed array is a crucial issue. The generator's utmost OAM order is contingent upon the number of unit cells, which establishes the resolution required to accommodate the required phase shift. Consequently, the array can be expanded to accommodate a sufficient number of unit cells in the event that a high OAM order is required. The proposed method offers a reliable and efficient approach to the generation of OAM modes at mm-wave frequencies.

#### FUNDING INFORMATION

Authors state no funding involved.

## AUTHOR CONTRIBUTIONS STATEMENT

This journal uses the Contributor Roles Taxonomy (CRediT) to recognize individual author contributions, reduce authorship disputes, and facilitate collaboration.

Name of Author	C	M	So	Va	Fo	I	R	D	O	E	Vi	Su	P	Fu
Nidal Qasem	✓	✓			✓	✓			✓	✓				

C : Conceptualization

M : Methodology

So : Software

Va : Validation

Fo : Formal analysis

I : Investigation

R : Resources

D : Data Curation

O : Writing - Original Draft

E : Writing - Review & Editing

Vi : Visualization

Su : Supervision

P : Project administration

Fu : Funding acquisition

## CONFLICT OF INTEREST STATEMENT

Authors state no conflict of interest.

## DATA AVAILABILITY

Derived data supporting the findings of this study are available from the author on request.

## REFERENCES




- [1] A. E. Willner, K. Pang, H. Song, K. Zou, and H. Zhou, "Orbital angular momentum of light for communications," *Applied Physics Reviews*, vol. 8, no. 4, pp. 041312, 2021, doi: 10.1063/5.0054885.
- [2] R. Chen, H. Zhou, M. Moretti, X. Wang, and J. Li, "Orbital angular momentum waves: generation, detection and emerging applications," *IEEE Access*, vol. 22, no. 2, pp. 840–868, 2020, doi: 10.1109/COMST.2019.2952453
- [3] A. Alamayreh, N. Qasem, and J. S. Rahhal, "General configuration MIMO system with arbitrary OAM," *Electromagnetics*, vol. 40, pp. 343–353, 2020, doi: 10.1080/02726343.2020.1780378.
- [4] D. Isakov, Y. Wu, B. Allen, P. S. Grant, C. J. Stevens, and G. J. Gibbons, "Evaluation of the laguerre– gaussian mode purity produced by three-dimensional-printed microwave spiral phase plates," *Royal Society Open Science*, vol. 7, no. 7, pp. 1–10, 2020, doi: 10.6084/m9.figshare.c.5063426.
- [5] Y. -M. Zhang and J. -L. Li, "An orbital angular momentum-based array for in-band full-duplex communications," in *IEEE Antennas and Wireless Propagation Letters*, vol. 18, no. 3, pp. 417–421, 2019, doi: 10.1109/LAWP.2019.2893035.
- [6] F. Qin, S. Gao, W. C. Cheng, Y. Liu, H. L. Zhang, and G. Wei, "A high-gain transmitarray for generating dual-mode OAM beams," *IEEE Access*, vol. 6, pp. 61006–61013, 2018, doi: 10.1109/ACCESS.2018.2875680.
- [7] M. Xin *et al.*, "Full control of dual-band vortex beams using a high-efficiency single-layer bi-spectral 2-bit coding metasurface," *Optics express*, vol. 28, no. 12, pp. 17374–17383, 2020, doi: 10.1364/OE.394571.
- [8] M. M. Sideeq and N. Qasem, "Smart wall based on active FSS wallpaper," *ZANCO Journal of Pure and Applied Sciences*, vol. 28, no. 2, pp. 1–6, 2016, doi: 10.21271/zjpas.v28i2.841.
- [9] Y. Wang *et al.*, "Planar vortex beam generator for circularly polarized incidence based on FSS," in *IEEE Transactions on Antennas and Propagation*, vol. 68, no. 3, pp. 1514–1522, March 2020, doi: 10.1109/TAP.2019.2938666.
- [10] M. R. Akram, X. Bai, R. Jin, G. A. E. Vandenbosch, M. Premaratne and W. Zhu, "Photon spin hall effect-based ultra-thin transmissive metasurface for efficient generation of OAM waves," in *IEEE Transactions on Antennas and Propagation*, vol. 67, no. 7, pp. 4650–4658, July 2019, doi: 10.1109/TAP.2019.2905777.
- [11] S. Jiang, C. Chen, H. Zhang, and W. Chen, "Achromatic electromagnetic metasurface for generating a vortex wave with orbital angular momentum (OAM)," *Optics Express*, vol. 26, no. 5, pp. 6466–6477, 2018, doi: 10.1364/OE.26.006466.
- [12] Z. Yu, L. Shi, and Z. Xin, "Polarization conversion and OAM generation with a single transmitting metasurface," *Progress in Electromagnetics Research M*, vol. 115, pp. 129–140, 2023, doi: 10.2528/PIERM23012301.
- [13] M. Z. Iskandarani, "Effect of waiting time and number of slots on vehicular networking employing slotted ALOHA protocol," *International journal of intelligent engineering and systems*, vol. 17, no. 2, pp. 145–158, 2024, doi: 10.22266/ijies2024.0430.13.
- [14] M. Z. Iskandarani, "Vehicular connectivity analysis using enhanced quality slotted ALOHA (EQS-ALOHA)," *Lecture Notes in Networks and Systems*, vol. 1019, pp. 484–509, 2024, doi:10.1007/978-3-031-62273-1\_31.
- [15] N. Qasem and N. Raheem, "A compact multi-band notched characteristics UWB microstrip patch antenna with a single sheet of graphene," *Telkomnika (Telecommunication Computing Electronics and Control)*, vol. 18, no. 4, pp. 1708–1718, 2020, doi: 10.12928/Telkomnika.V18I4.14942.
- [16] H. M. Marhoon, N. Qasem, N. Basi, and A. R. Ibrahim, "Design and simulation of a compact metal-graphene frequency reconfigurable microstrip patch antenna with FSS superstrate for 5G applications," *International Journal on Engineering Applications*, vol. 10, no. 3, pp. 193–201, 2022, doi: 10.15866/irea.v10i3.21752.
- [17] X. Bai *et al.*, "Dynamic millimeter-wave OAM beam generation through programmable metasurface," *Nanophotonics*, vol. 11, no. 7, pp. 1389–1399, 2022, doi: 10.1515/nanoph-2021-0790.
- [18] B. Zheng, X. Rao, Y. Shan, C. Yu, J. Zhang, and N. Li, "Multiple-beam steering using graphene-based coding metasurfaces," *Micromachines*, vol. 14, no. 5, pp. 3–10, 2021, doi: 10.3390/mi14051018.
- [19] A. Cao, N. Chen, W. Zhu, and Z. Chen, "Graphene-based dual-band metasurface absorber with high frequency ratio," *Nanomaterials*, vol. 14, no. 18, pp. 1, 2024, doi: 10.3390/nano14181522.
- [20] R. Li *et al.*, "Ultra-thin circular polarization analyzer based on the metal rectangular split-ring resonators," *Opt Express*, vol. 22, no. 23, pp. 27968–27975, 2014, doi: 10.1364/OE.22.027968.



- [21] M. A. Al-Joumayly, and N. Behdad, "Wideband planar microwave lenses using sub-wavelength spatial phase shifters," *IEEE Transactions on Antennas and Propagation*, vol. 59, no. 12, pp. 4542–4552, 2011, doi: 10.1109/TAP.2011.2165515.
- [22] M. Li, M. A. Al-joumayly, and N. Behdad, "Broadband true-time-delay microwave lenses based on miniaturized element frequency selective surfaces," *IEEE Transactions on Antennas and Propagation*, vol. 61, no. 3, pp. 1166–1179, 2013, doi: 10.1109/TAP.2012.2227444.
- [23] M. Li and N. Behdad, "Wideband true-time-delay microwave lenses based on metallo-dielectric and all-dielectric lowpass frequency selective surfaces," *IEEE Transactions on Antennas and Propagation*, vol. 61, no. 8, pp. 4109–4119, 2013, doi: 10.1109/TAP.2013.2263784.
- [24] M. A. Al-Joumayly and N. Behdad, "A generalized method for synthesizing low-profile, band-pass frequency selective surfaces with non-resonant constituting elements," *IEEE Transactions on Antennas and Propagation*, vol. 58, no. 12, pp. 4033–4041, 2010, doi: 10.1109/TAP.2010.2078474.
- [25] A. Patnaik and S. Dash, "Graphene loaded frequency reconfigurable metal antenna," *IEEE International Conference on Antenna Innovations and Modern Technologies for Ground, Aircraft and Satellite Applications (iAIM)*, Bangalore, India, 2017, pp. 1–4, doi: 10.1109/IAIM.2017.8402579.
- [26] N. Qasem and H. M. Marhoon, "Simulation and optimization of a tuneable rectangular microstrip patch antenna based on hybrid metal-graphene and FSS superstrate for fifth-generation applications," *Telkomnika (Telecommunication Computing Electronics and Control)*, vol. 18, no. 4, pp. 1719–1730, 2020, doi: 10.12928/telkomnika.v18i4.14988.
- [27] C. N. Alvarez, R. Cheung, and J. S. Thompson, "Performance analysis of hybrid metal-graphene frequency reconfigurable antennas in the microwave regime," *IEEE Transactions on Antennas and Propagation*, vol. 65, no. 4, pp. 1558–1569, 2017, doi: 10.1109/TAP.2017.2670327.
- [28] B. Jack, M. J. Padgett, and S. F. Arnold, "Angular diffraction," *New Journal of Physics*, vol. 10, no. 10, p. 103013, 2008, doi: 10.1088/1367-2630/10/10/103013.
- [29] M. Lin *et al.*, "Single-layer re-organizable all-dielectric meta-lens platform for arbitrary transmissive phase manipulation at millimeter-wave frequencies," *IEEE Transactions on Antennas and Propagation*, vol. 70, no. 3, pp. 2059–2069, 2022, doi: 10.1109/TAP.2021.3111163.
- [30] Y. Wang *et al.*, "Generation of high-efficiency vortex beam carrying OAM mode based on miniaturized element frequency selective surfaces," *IEEE Transactions on Magnetics*, vol. 55, no. 10, pp. 1–4, 2019, doi: 10.1109/TMAG.2019.2919715.
- [31] F. Qin, R. Song, W. Cheng, and H. Zhang, "Multibeam OAM transmitarray with stable vortex property based on bifocal method," *IEEE Antennas and Wireless Propagation Letters*, vol. 20, no. 9, pp. 1601–1605, 2021, doi: 10.1109/LAWP.2021.3084604.
- [32] X. Wang, Y. Chen, S. Zheng, and X. Zhang, "Reconfigurable OAM antenna based on sub-wavelength phase modulation structure," *IET Microwaves Antennas & Propagation*, vol. 12, no. 3, pp. 354–359, 2018, doi: 10.1049/iet-map.2017.0629.

## BIOGRAPHIES OF AUTHORS



**Nidal Qasem**    received his B.Sc. degree in Electronics and Communications Engineering (Honours) from Al-Ahliyya Amman University, Amman, Jordan, in 2004. He obtained his M.Sc. degree in Digital Communication Systems for Networks and Mobile Applications (DSC) in 2006, followed by a Ph.D. in Wireless and Digital Communication Systems, both from Loughborough University, Loughborough, United Kingdom. He currently holds the position of full professor in the department of Communications and Computer Engineering at Al-Ahliyya Amman University. His research interests include propagation control in buildings, specifically improving the received power, FSS measurements and designs, antennas, ultra-wide band, orbital angular momentum, and wireless system performance analyses. He can be contacted at email: ne.qasem@ammanu.edu.jo.